Mon. Not. R. Astron. Soc. **000**, 000–000 (0000) Printed 17 May 2006 (MN LATEX style file v2.2)

Gas distribution, kinematics and star formation in faint dwarf galaxies

Ayesha Begum[1⋆], Jayaram. N. Chengalur[1], I. D. Karachentsev[2], S. S. Kaisin[2] and M. E. Sharina[2]

[1]*National Centre for Radio Astrophysics, Post Bag 3, Ganeshkhind, Pune 411 007, India*
[2]*Special Astrophysical Observatory, Nizhnii Arkhys 369167, Russia*

arXiv:astro-ph/0511253 v1 9 Nov 2005

ABSTRACT

We compare the gas distribution, kinematics and the current star formation in a sample of 10 very faint ($-13.37 < \mathrm{M_B} < -9.55$) dwarf galaxies. For 5 of these galaxies we present fresh, high sensitivity, GMRT HI 21cm observations. We find that the large scale HI distribution in the galaxies is typically irregular and clumpy, with the peak gas density rarely occurring at the geometric center. We also find that the velocity fields for all the galaxies have an ordered component, although in general, the patterns seen do not fit that expected from a rotating disk. For all our galaxies we construct maps of the HI column density at a constant linear resolution of ~ 300 pc; this forms an excellent data set to check for the presence of a threshold column density for star formation. We find that while current star formation (as traced by Hα emission) is confined to regions with relatively large ($\mathrm{N_{HI}} > (0.4 - 1.7) \times 10^{21}$ cm^{-2}) HI column density, the morphology of the Hα emission is in general not correlated with that of the high HI column density gas. Thus, while high column density gas may be necessary for star formation, in this sample at least, it is not sufficient to ensure that star formation does in fact occur. We examine the line profiles of the HI emission, but do not find a simple relation between regions with complex line profiles and those with on-going star formation. Our sample includes examples of regions where there is on-going star formation, but the profiles are well fit by a single Gaussian, as well as regions where there is no star formation but the line profiles are complex. Finally, we examine the very fine scale ($\sim 20 - 100$ pc) distribution of the HI gas, and find that at these scales the emission exhibits a variety of shell like, clumpy and filamentary features. The Hα emission is sometimes associated with high density HI clumps, sometimes the Hα emission lies inside a high density shell, and sometimes there is no correspondence between the Hα emission and the HI clumps. In summary, the interplay between star formation and gas density in these galaxy does not seem to show the simple large scale patterns observed in brighter galaxies.

Key words: galaxies: dwarf – galaxies: individual: UGC 4459 galaxies: individual: UGC 7298 galaxies: individual: KDG 52 galaxies: individual: CGCG 269-049 radio lines: galaxies

1 INTRODUCTION

In the currently popular hierarchical models of galaxy formation, star formation starts in small objects; these in turn later merge to form larger galaxies. In such a model, extremely small nearby galaxies are likely candidate "primeval galaxies", in the sense that they may represent the earliest units of star formation in the universe. There is some observational support for these models, even in the very local universe, viz. (i) the Milkyway itself appears to be still growing via the accretion of small companions like the Sagittarius dwarf galaxy (see e.g. Majewski et al.(2003)), and (ii) nearby dwarf galaxies have stellar populations that are at least as old as the oldest stars in the Milkyway (see Grebel (2005) for a recent review).

In detail, however, the star formation history of nearby dwarf galaxies appears to be extremely varied. At the two extreme ends, dwarf spheroidals have little gas or ongoing star formation while the relatively rare dwarf irregulars are gas rich and also generally have measurable ongoing star formation. Their past star formation histories also appear to have been different – at a given luminosity

⋆ E-mail:ayesha@ncra.tifr.res.in

dwarf spheroidals are more metal rich than dwarf irregulars, indicative of rapid chemical enrichment in dwarf spheroidals in the past (Grebel (2004)). Why is it that dwarf irregulars, despite having a substantial reservoir of gas have resisted converting it into stars? What keeps the gas in dwarf irregulars from collapse? It is widely believed that the smallest dwarf irregular galaxies have chaotic gas velocity fields (e.g. Lo et al.(1993)), in this case the crucial question then becomes, what sustains these chaotic gas motions? In this context, it is interesting to note that for galaxies which have been observed with sufficient sensitivity and velocity resolution, the velocity field has invariably turned out to have a measurable ordered component, (Begum et al.(2003), Young et al.(2003), Begum & Chengalur (2004)). Does this generally hold for extreme dwarf irregulars, or do some of them genuinely have no ordered components in their velocity fields? Irrespective of the exact nature of the velocity fields, the question of why dwarf irregulars have been unable to convert their gas into stars remains. In spiral galaxies, the current star formation rate appears to depend on at most two parameters (i) the gas surface density and (ii) some measure of the dynamical time. In practice, models which depend only on the gas surface density, such as the Schmidt star formation law, or those which depend on both these parameters, such as the Toomre's instability criterion (Toomre (1964)) appear to provide an equally good fit to the observations (Kennicutt (1998)). For irregular galaxies, Skillman (1987) has proposed that star formation occurs only above a threshold column density, and that this threshold may be related to a critical amount of dust shielding required for molecular gas formation. Are any of these models extrapolatable to the faintest dwarf irregulars?

We present here deep, high velocity resolution (~ 1.6 km s^{-1}) Giant Metrewave Radio Telescope (GMRT) HI observations, as well as Hα observations of a sample of faint ($M_B \widetilde{>} -13.0$ mag) galaxies, aimed at addressing the above issues. The rest of the paper is divided as follows. The dwarf galaxy sample is presented in Sect. 2, the GMRT observations are detailed in Sect. 3, while the results are presented in Sect. 4 and discussed in Sect. 5.

2 DWARF GALAXY SAMPLE

The optical properties of our sample of ten galaxies are given in Table 1. Fresh HI observations for five galaxies in the sample viz. KDG 52, UGC 4459, CGCG 269-049, UGC 7298 and KK 230 are presented in this paper. GMRT HI data for KK 44 (Camelopardalis B), GR 8 and DDO 210 were presented in our previous papers (Begum et al.(2003), Begum & Chengalur (2003,2004)), although we include here fresh maps and measurements at angular scales that are relevant to the issues discussed in this paper. GR 8 and DDO 210 were also observed with the VLA; the VLA data for these galaxies are presented in Young et al.(2003). VLA HI data for Sag DIG and Leo A were obtained from the VLA archive. These observations have been discussed earlier by Young & Lo (1996) (Leo A) and Young et al.(1997) (Sag DIG); once again we present here only those maps and measurements that are relevant to this paper.

3 OBSERVATIONS AND ANALYSIS

3.1 Optical observations and data analysis

Hα observations of some of our sample galaxies, viz. KK 44, KDG 52, CGCG 269-049, UGC 7298 & KK 230 were carried out at the 6-meter SAO telescope using a 2048×2048 pixel CCD camera. The scale was 0.36 $''$/pixel, and the total area imaged was $6\times6'$. The Hα + [NII] emission line fluxes were obtained by observing each galaxy through two filters: a narrow ($\sim$75 Å) interference filter centered on 6567 Å, and a middle-width filter (λ = 6063 Å, $\Delta\lambda$ = 167 Å) to determine the nearby continuum level. The integration times were 2×300 sec in the middle-width filter and 2×600 sec in Hα. Because the range of radial velocities was small, we used the same Hα filter for all objects. The images were bias subtracted and flat fielded following standard procedures. After flat fielding, the next step was to subtract the sky emission from both continuum and narrow band filter images. The continumm filter images were then scaled relative to the narrow band images using 5–10 unsaturated stars, and then subtracted from the narrow band filter images. The continuum-subtracted Hα images were flux calibrated using observations from the same night of two or more of Feige's photometric standards. Corrections for the Galactic extinction were made assuming A(Hα)= 2.32 E(B-V) using the data from Schlegel et al. (1998). The star formation rate for these galaxies were calculated from the derived Hα luminosities, using the conversion factor from Kennicutt (1998a)

$$\mathrm{SFR} = 7.9 \times 10^{-42}\, \mathrm{L(H\alpha)}\, \mathrm{M_\odot yr^{-1}} \quad (1)$$

The calculated SFR for our sample galaxies are given in Table 5. In case of KDG 52 and KK 230, no Hα emission was detected; the derived limits on the SFR for these galaxies is also listed in Table 5.

For Leo A, Sag DIG and GR 8, Hα images were downloaded from NED. Details of these images can be found in Hunter & Elmegreen (2004). The Hα image of UGC 4459 was kindly provided by U. Hopp; details can be found in Schulte-Ladbeck & Hopp (1998). For DDO 210, van Zee (2000) detected a single source of Hα emission in the galaxy; however follow up observations suggested that it does not arise in a normal HII region, but probably comes from dense outflowing material from an evolved star. In all the figures of DDO 210 in this paper, we show the location of this emission by a star, but caution the reader that it may not actually represent a star forming region.

Except for KK 230, broadband optical observations of all our sample galaxies were available in the literature. For KK 230, V and I band HST ACS images were used to obtain the total magnitude of the galaxy. The derived magnitude is $\mathrm{I}(\mathrm{R} < 40'') = 15\overset{\mathrm{m}}{.}6 \pm 0\overset{\mathrm{m}}{.}15$, and the integrated $(\mathrm{V}-\mathrm{I})$ colour inside the same radius is 0.90. Assuming a typical color $(\mathrm{B}-\mathrm{V}) = 0.50$ for KK 230, we estimated its integrated blue magnitude to be $\mathrm{B} = 17\overset{\mathrm{m}}{.}0 \pm 0\overset{\mathrm{m}}{.}25$.

3.2 HI observations and data analysis

HI 21cm observations of KDG 52, UGC 4459, CGCG 269-049, UGC 7298 and KK 230 were conducted with the GMRT (Swarup et al. (1991)) between Nov. 2001 and Nov. 2002. KK 44, GR 8 and DDO 210 were also observed with the GMRT; details can be found in Begum et al.(2003), Begum & Chengalur (2003,2004). Data for Sag DIG and Leo A were obtained from the VLA archive. These observations are also discussed in Young & Lo (1996,1997). Here we briefly describe only the fresh GMRT observations.

For all galaxies, the observing bandwidth of 1 MHz was divided into 128 spectral channels, yielding a spectral resolution of 7.81 kHz (velocity resolution of 1.65 km s^{-1}). The setup for the observations is given in Table 2. The flux and bandpass calibration were done using 3C48, 3C147 and 3C286. The phase calibration was done once in every 30 min by observing the VLA calibrator

Table 1. Optical parameters of the sample galaxies

Galaxy	RA(J2000)	Dec(J2000)	M_B	D (Mpc)	B-V	R_{Ho} ($'$)	$i_{opt}(^\circ)$	references
KK 44	$04^h53^m06.9^s$	$+67^\circ05'57''$	-11.85	3.34	0.8	0.7	65	1,3
KDG 52	$08^h23^m56.0^s$	$+71^\circ01'46''$	-11.49	3.55	0.24	0.65	24	3
UGC 4459	$08^h34^m06.5^s$	$+66^\circ10'45''$	-13.37	3.56	0.45	0.80	30	3,7
Leo A	$09^h59^m26.4^s$	$+30^\circ44'47''$	-11.36	0.69	0.15	3.5	54	3,4,8
CGCG 269-049	$12^h15^m46.7^s$	$+52^\circ23'15''$	-12.46	3.4	-	0.60	77	3
UGC 7298	$12^h16^m28.6^s$	$+52^\circ13'38''$	-12.27	4.21	0.29	0.55	58	3,7
GR 8	$12^h58^m40.4^s$	$+14^\circ13'03''$	-12.11	2.10	0.32	0.95	25	2,3
KK 230	$14^h07^m10.7^s$	$+35^\circ03'37''$	-9.55	1.9	0.40	0.87	35	3
Sag DIG	$19^h29^m59.0^s$	$-17^\circ40'41''$	-11.49	1.1	0.3	1.8	45	3,6
DDO 210	$20^h46^m51.8^s$	$-12^\circ50'53''$	-11.09	1.0	0.24	1.8	62	3,5

References: 1-Begum et al. (2003), 2-de Vaucouleurs & Moss (1983), 3-Karachentsev et al.(2004), 4- Karachentseva & Sharina (1988) 5-Lee et al.(1999), 6-Lee & Kim (2000), 7-Makarova (1999), 8-Tolstoy et al. (1998)

Table 2. Parameters of the GMRT observations

Galaxy	Date of observations	Velocity coverage (km s^{-1})	Time on source (hours)	synthesised beam (arcsec^2)	synthesised beam (pc^2)	Noise (mJy)	Continuum Noise (3σ) ($26'' \times 22''$),($3'' \times 3''$) (mJy)
KDG 52	21-23, 27, Jun 2002	$10-220$	18	$42'' \times 39''$,$26'' \times 23''$ $16'' \times 15''$, $6'' \times 6''$	723×671, 447×396 275×258, 103×103	1.7,1.5 1.3,0.9	0.9, 0.42
UGC 4459	15, 23, 24, Nov 2002	$-60-130$	14	$45'' \times 38''$,$29'' \times 27''$ $18'' \times 16''$,$3'' \times 3''$	777×656,500×466 310×276,52×52	1.9,1.6 1.4,1.2	1.0, 0.45
CGCG 269-049	23−25, Nov 2002	$65-275$	16	$42'' \times 39''$,$28'' \times 24''$ $18'' \times 17''$,$4'' \times 3''$	692×642, 461×396 297 × 280, 66×50	2.0,1.8 1.7,1.2	0.5, 0.3
UGC 7298	23−25, Nov 2002	$65-275$	16	$42'' \times 37''$,$26'' \times 24''$ $16'' \times 15''$,$4'' \times 4''$	857×755, 530 ×490 326 ×306, 82×82	2.0,1.8 1.6,1.1	0.5, 0.3
KK 230	6 Jun, 8 May, 26 Nov 2001	$-40-170$	18	$48'' \times 45''$,$34'' \times 31''$ $26'' \times 24''$,$4'' \times 3''$	442× 415,313×286 240×221, 37×28	1.6,1.4 1.2,0.8	0.4, 0.2

sources 0831+557 (UGC 4459), 1216+487 (UGC 7298), 1216+487 (CGCG 269-049), 3C286 (KK 230) and 0834+555 (KDG 52). The galaxies UGC 7298 and CGCG 269-049 are close in space ($\sim 12'$) as well as in velocity, hence both were included in a single GMRT pointing (the field of view of the GMRT $\sim 24'$).

The data were reduced in the usual way using standard tasks in classic AIPS. For each run, bad visibility points were edited out, after which the data were calibrated. The GMRT does not do online doppler tracking – any required doppler shifts have to be applied during the offline analysis. For UGC 7298 and CGCG 269-049, the differential doppler shift over our observing interval was much less than the channel width, hence, there was no need to apply any offline correction. On the other hand, the differential shifts for UGC 4459, KK 230 and KDG 52 were significant, hence, for each of these galaxies, the calibrated (u,v) data set for each day was shifted in the frequency space to the heliocentric velocity of the galaxy, using the task CVEL in AIPS. For each galaxy, data for all the runs were then combined using the AIPS task DBCON.

The GMRT has a hybrid configuration (Swarup et al. (1991)) which simultaneously provides both high angular resolution ($\sim 3''$, if one uses baselines between the arm antennas) as well as sensitivity to extended emission (from baselines between the antennas in the central array). Data cubes were therefore made using various (u,v) cutoffs to get the images of HI emission at various spatial resolutions (see Table 2 for details). Except for the highest resolution HI data cubes for each galaxy, all the data cubes were deconvolved using the AIPS task IMAGR. For the highest resolution data cubes in each galaxy, the signal to noise ratio (SNR) was too low for CLEAN to work reliably. Despite this, the low SNR of the images implies that the inability to deconvolve does not greatly degrade the dynamic range or fidelity of these images. The morphology of the emission in these galaxies should hence be accurately traced, apart from an uncertainty in the scaling factor (this essentially arises because the main effect of deconvolving weak emission at about the noise level corresponds to multiplying by a scale factor; see e.g. Jörsäter & van Moorsel (1995), Rupen (1999)).

Continuum images were also made for all the galaxies by averaging the line free channels. No extended ($26'' \times 22''$) or compact ($3'' \times 3''$) emission was detected from any of the galaxies. The 3σ limits for each galaxy are given in Table 2.

Moment maps were made from the data cubes using the AIPS task MOMNT. Maps of the velocity field and velocity dispersion were also made in GIPSY using single Gaussian fits to the individual profiles. The velocity field produced by Gaussian fitting is in reasonable agreement with that obtained from moment analysis. The velocity dispersion ($\sigma_{\rm obs}$), as estimated by fitting single Gaussian component to the line profiles is given in Table 3. In all cases, no measurable variation of velocity dispersion was seen (within the errorbars) across each galaxy. This lack of substantial variation of σ across each galaxy is typical of such faint dwarf irregular galaxies (e.g. Begum & Chengalur (2004), Begum et al. (2003), Skillman et al. (1988)). As discussed in more detail in section 5.3, single Gaus-

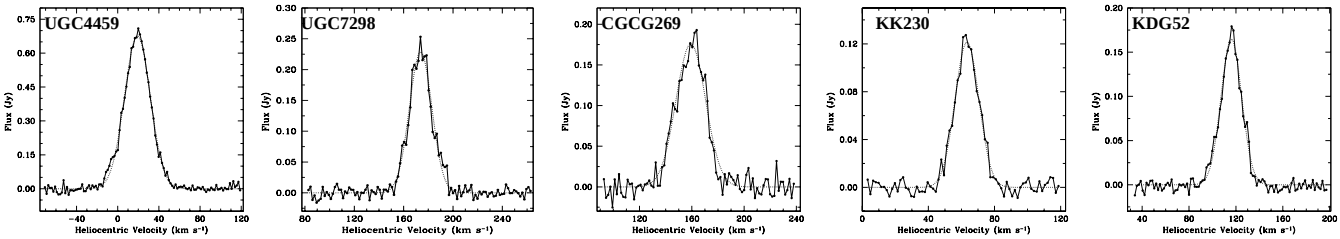

Figure 1. The HI global profile for our sample galaxies derived from our coarsest resolution HI distribution. The channel separation is 1.65 km s^{-1}. The dotted line shows a Gaussian fit to the line profiles.

sian profiles are not necessarily a good fit throughout the galaxy; there are regions where the emission profile is skewed or is otherwise more complex than a single Gaussian.

4 RESULTS

4.1 Large scale HI distribution and kinematics

The global HI profiles for our sample galaxies, obtained from the coarsest resolution data cubes (see Table 2) are shown in Fig. 1. Column (2−7) in Table 3 lists the parameters derived from the global HI profiles. Col. (1) gives the galaxy name, (2) the integrated HI flux along with the errorbars, (3) the velocity width at 50% of the peak (ΔV_{50}), along with the errorbars, (4) the central heliocentric velocity ($V_\odot$) and its errorbars, (5) the HI mass along with its errorbars, (6) the HI mass-to-light ratio (M_{HI}/L_B), (7) the ratio of the GMRT flux to the single dish flux (FI/FI_{SD}). The single dish fluxes for all the galaxies are taken from the tabulation in Karachentsev et al.(2004). In the case of CGCG 269-049, single dish data is not available. The parameters measured from the GMRT HI profiles are in good agreement with those values obtained from the single dish observations, in particular the HI flux measured at the GMRT agrees with the single dish flux for all the galaxies. This indicates that no flux was missed because of the missing short spacings in our interferometric observations. Col.(8) shows the velocity dispersion, along with error bars, as measured from a single Gaussian fit to the line profiles, (9) represents the HI radius at a column density of 10^{19} atoms cm^{-2}, (10) the inclination as measured from the HI moment 0 maps, (11) the ratio of the HI diameter to the Holmberg diameter. For all the galaxies the HI emission extends to $\sim 2-3$ times the optical diameter, a typical ratio for dwarf irregular galaxies.

The integrated HI emission of our sample galaxies overlayed on the optical Digitized Sky Survey (DSS) images are shown in Fig.3[A]- 7[A]. The HI distribution in CGCG 269-049 and KK 230 are dominated by a single clump of high column density, while the HI in UGC 4459 and UGC 7298 are concentrated in two high-column-density regions, separated by a low-column density region in the center. In the case of KDG 52, the HI is distributed in a clumpy, incomplete ring.

Inclinations (i_{HI}) of our sample galaxies (except for KDG 52) were estimated from the HI moment 0 maps by fitting elliptical annuli to the two lowest resolution images. For KDG 52, only the lowest resolution HI distribution is sufficiently smooth to be used for ellipse fitting. For all other galaxies, the inclination derived from these two resolution images match within the errorbars. The estimated inclination for each galaxy (assuming an intrinsic thickness $q_o = 0.2$) is tabulated in Table 3. Comparing this value to the optical inclination (Table 1), shows that the two inclinations are in agreement for UGC 4459 and KDG 52, whereas for the rest of the sample galaxies the optical inclination is either found to be much higher (UGC 7298 and CGCG 269-049) or lower (KK 230) than the inclinations derived from the HI morphology. Using the derived HI inclination, the deprojected HI radial surface mass density profiles (SMD) for each galaxy were obtained by averaging the HI distribution over elliptical annuli in the plane of the galaxy. The derived SMD profiles for each galaxy are given in Fig. 2.

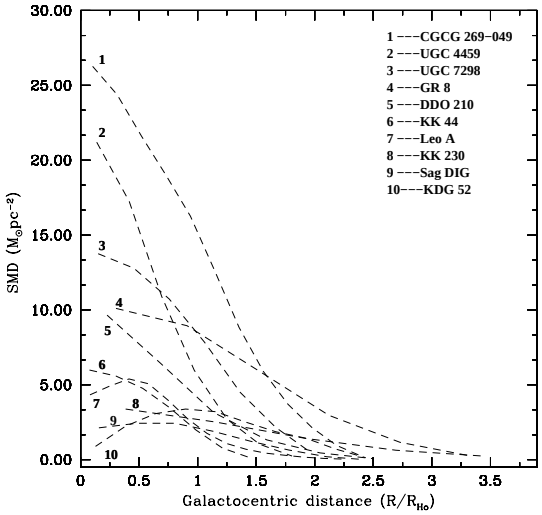

Figure 2. The deprojected gas surface mass density (SMD) distribution for our sample galaxies. For all galaxies (except DDO 210, Sag DIG and Leo A), the SMD was computed for a linear resolution of $\sim$ 500 pc. For DDO 210, Sag DIG and Leo A the linear resolution is $\sim$ 300 pc. The actual angular resolutions are 29 $''$ × 27$''$ (UGC 4459), 26$''$ × 24$''$ (UGC 7298), 28$''$ × 24$''$ (CGCG 269-049), 48$''$ × 45$''$ (KK 230), 26$''$ × 23$''$ (KDG 52),41$''$ × 39$''$ (GR 8), 61$''$ × 56$''$ (DDO 210), 31$''$ × 29$''$ (KK 44), 67$''$ × 65$''$ (Sag DIG) and 78$''$ × 72$''$ (Leo A). The gas SMD is obtained by scaling the HI SMD profile by 1.4 to account for primordial He.

We next discuss in detail the large scale HI distribution and kinematics for the five galaxies for which fresh GMRT observations are presented in the current paper. For similar details on the other galaxies in our sample, the reader is referred to Begum et al.(2003), Begum & Chengalur (2003,2004) and Young & Lo (1996,1997).

Table 3. Results from GMRT observations

Galaxy	FI (Jy km s^{-1})	ΔV_{50} (km s^{-1})	$V_\odot$ (km s^{-1})	M_{HI} ($10^6 M_\odot$)	M_{HI}/L_B	FI/FI_{SD}	σ_{obs} (km s^{-1})	R_{HI} ($'$)	i_{HI} ($^\circ$)	R_{HI}/R_{Ho}
KK 44	4.6(0.4)	21.4(1.0)	77.5(1.0)	12.2(1.2)	1.4	1.02	7.3(0.8)	1.6	65	2.3
Leo A	42.0(4.0)	18.8(0.7)	21.7(0.7)	4.7(0.4)	1.02	0.88	9.5(1.3)	8.0	62	2.3
KDG 52	3.8(0.4)	20.6(1.7)	116.0(1.9)	10.8(1.1)	1.8	0.85	9.0(1.0)	1.8	23	2.7
UGC 4459	21.5(2.2)	29.6(1.8)	19.2(2.3)	64.2(6.5)	1.4	1.01	9.0(1.6)	2.2	31	2.8
CGCG 269-049	4.7(0.5)	26.6(2.2)	159.0(3.4)	12.7(1.3)	0.9	–	9.5(1.0)	1.3	43	2.3
UGC 7298	5.2(0.5)	21.4(1.7)	174.0 (2.0)	21.6(2.1)	1.7	1.06	8.5(1.3)	1.8	28	3.1
GR 8	9.0(0.9)	26.0(1.2)	217.0(2.2)	10.38(1.0)	1.02	1.03	9.0(0.8)	2.1	28	2.3
KK 230	2.2(0.2)	17.0(2.0)	63.3(1.8)	1.9(0.2)	1.9	0.86	7.5(0.5)	1.5	51	3.3
Sag DIG	23.0(1.0)	19.4(0.8)	−78.5(1.0)	5.4(0.2)	1.02	0.92	7.5(1.7)	2.1	33	2.3
DDO 210	12.1(1.2)	19.1(1.0)	−139.5(2.0)	2.8(0.3)	1.00	1.05	6.5(1.0)	2.4	27	1.3

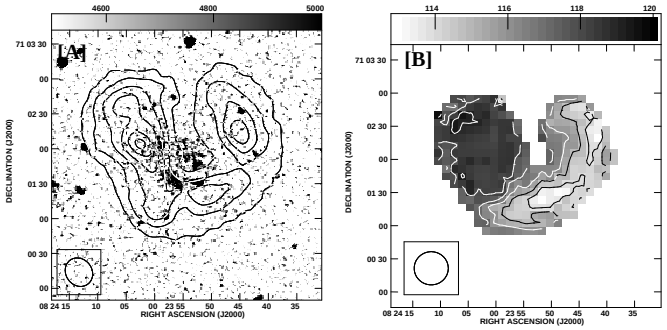

Figure 3. [A] The B band optical DSS image of KDG 52 (greyscales) with the GMRT $26'' \times 23''$ resolution integrated HI emission map (contours) overlayed. The contour levels are 0.25, 1.00, 1.75, 2.49, 3.10 & 3.67 $\times 10^{20}$ atoms cm^{-2}. **[B]** The velocity field of the galaxy at $26'' \times 23''$ resolution. The contours are in the steps of 1.0 km s^{-1}and range from 113.0 km s^{-1}to 118.0 km s^{-1}.

4.2 Notes on individual galaxies

4.2.1 KDG 52

KDG 52 (also called M81DwA) was discovered by Karachentseva(1968) and was later detected in HI by Lo & Sargent (1979). The neutral hydrogen in this galaxy is distributed in a clumpy, broken ring surrounding the optical emission (Fig. 3[A]). The central HI hole has a diameter of $\sim 40''$ ($\sim$ 688 pc); similar central HI holes are seen in other faint dwarf galaxies (e.g. Sag DIG; Young & Lo (1997), DDO 88; Simpson et al. (2005)). The HI hole is not exactly centered on the optical emission; the HI column density at the eastern side of the optical emission is $N_{HI} \sim 4 \times 10^{20}$ atoms cm^{-2}, while the rest of the optical emission lies inside the HI hole. Prior to this work, there have been two HI interferometric studies of KDG 52. It was observed with the WSRT by Sargent et al.(1983) with a velocity resolution of $\sim$ 8 km s^{-1}and later re-observed with a high velocity resolution in the C array of the VLA (Westpfahl et al. (1999)). The overall morphology of the earlier images compares well with that of our image.

Our coarsest resolution HI distribution and velocity field (not shown) shows faint emission in the center and in the northern region of the galaxy, a feature that is not visible at the higher resolutions. One may suspect that this HI emission is not real but is the result of beam smearing. To check for this possibility, the individual channel maps in the $42'' \times 39''$ data cube were inspected. In the channel maps, the peak of the diffuse emission in the central as well as in the northern region in the galaxy occurs at the same heliocentric velocity as that of nearby HI clumps, suggesting that they may arise due to beam smearing. As a further check, the clean components from the $42'' \times 39''$ resolution data cube were convolved with a smaller restoring beam of $30'' \times 30''$, to generate a new data cube. The diffuse emission which was visible in $42'' \times 39''$ data cube is not seen in the channel maps in this cube, i.e. no clean components were found in the region of diffuse emission. Finally, the HI flux measured from a genuine $30'' \times 30''$ resolution data cube (i.e. made from the visibility data by applying the appropriate UV range and taper) is the same as that measured from the $42'' \times 39''$ data cube. All these indicate that the diffuse emission in $42'' \times 39''$ is entirely due to beam smearing.

The velocity field obtained from $26'' \times 23''$ resolution data cube is given in Fig. 3[B]. The velocity field shows a large scale gradient across the galaxy with a magnitude of $\sim$ 1.7 km s^{-1}kpc^{-1}. However the velocity field is clearly not consistent with pure rotation. One can still crudely estimate the maximum possible circular velocity in the following way; the velocity difference from one edge of the galaxy to the other is $\sim$ 6 km s^{-1}, this implies that the magnitude of any circular velocity component must be limited to $V_{rot}\sin(i) \leqslant 3$ km s^{-1}. Puche & Westpfahl (1994) have tried to model this velocity field, and find that a combination of rotation (with a magnitude of 7 km s^{-1}) and expansion (with a magnitude of 5 km s^{-1}) provides a reasonable fit. A similar combination of rotation and expansion was found to provide a good fit to the kinematics of another of our sample galaxies, viz. GR 8 (Begum & Chengalur (2003)).

KDG 52 is a member of M81 group of galaxies. Bureau et al.(2004), have suggested that this galaxy is probably a tidal dwarf, formed through gravitational collapse of the tidal debris from the previous interactions of Holmberg II with UGC 4483. In Sec. 5.1, we estimate the dynamical mass of this galaxy from the virial theorem; this mass estimate implies that the galaxy has a significant amount of dark matter. This would argue against a tidal dwarf origin for KDG 52, since tidal dwarfs are generally not expected to be dark matter dominated (e.g. Braine et al.(2002)).

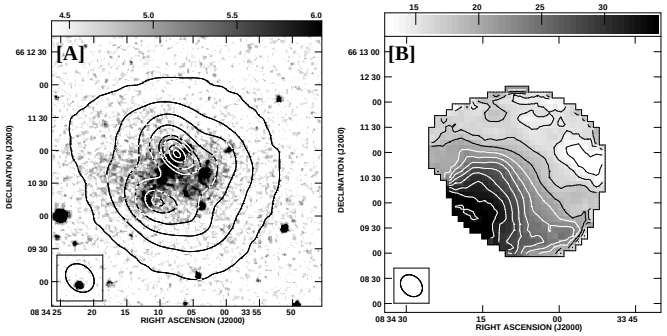

Figure 4. [A] The B band optical DSS image of UGC 4459 (greyscales) with the GMRT $29'' \times 27''$ resolution integrated HI emission map (contours) overlayed. The contour levels are 0.22, 3.33, 6.45, 9.56, 12.67, 15.79, 18.91, 22.00, 24.12, 28.25 and 31.36 $\times 10^{20}$ atoms cm^{-2}. **[B]** The HI velocity field for galaxy at $29'' \times 27''$ resolution. The contours are in the steps of 2.0 km s^{-1}and range from 13.0 km s^{-1}to 33.0 km s^{-1}.

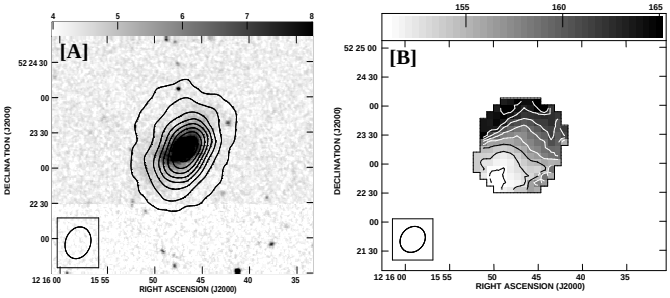

Figure 5. [A] The B band optical DSS image of CGCG 269-049 (greyscales) with the GMRT $28'' \times 24''$ resolution integrated HI emission map (contours) overlayed. The contour levels are 0.08, 1.12, 2.18, 3.23, 4.28, 5.33, 6.39, 7.44, 8.49 and 9.55 $\times 10^{20}$ atoms cm^{-2}. **[B]** The HI velocity field for galaxy at $28'' \times 24''$ resolution. The contours are in the steps of 2.0 km s^{-1}and range from 151.0 km s^{-1}to 165.0 km s^{-1}.

4.2.2 UGC 4459

UGC 4459 is a member of M81 group of galaxies. It is relatively metal poor, with 12+log(O/H)$\sim$ 7.62 (Kunth & Östlin (2000)). The optical appearance of UGC 4459 is dominated by bright blue clumps, which emit copious amounts of Hα (Fig. 4[A], 9 & 12). The two high density peaks seen in the integrated HI map coincide with these star forming regions (Fig. 4[A]).

The velocity field of UGC 4459 (Fig. 4[B]) shows a large scale gradient (aligned along the line connecting the two star forming regions) across the galaxy. The magnitude of the average velocity gradient across the whole HI disk is ~ 4.5 km s^{-1}kpc^{-1}. However we note that the gradient is not uniform across the galaxy. The receding (southeastern) half of the galaxy shows a rapid change in velocity with galacto-centric distance, while the approaching (northwestern) half of the galaxy shows a much more gentle gradient. UGC 4459 is a fairly isolated dwarf galaxy with its nearest neighbor UGC 4483 at a projected distance of 3.6°($\sim$ 223 kpc) and at a velocity difference of 135 km s^{-1}. Being a member of the M81 group, it is possible that interaction with intra-group gas could produce such disturbed kinematics. To check for this possibility, we estimated the ram pressure required to strip gas from this galaxy. The threshold condition for ram pressure stripping is given by (Gunn & Gott (1972))

$$\rho_{\rm IGM} v^2 \geqslant 2\pi G \Sigma_* \Sigma_{\rm g} \qquad (2)$$

where, $\rho_{\rm IGM}$ is the density of the intra-group medium (IGM) and v is the relative velocity of the galaxy moving through the IGM. Σ_* and $\Sigma_{\rm g}$ are stellar and gas surface density respectively. Taking $v \sim 190$ km s^{-1}, typical for M81 group (Bureau & Carignan (2002)), and values for Σ_* and $\Sigma_{\rm g}$ from the location in the galaxy where the velocity field begins to look perturbed, we find that the IGM volume density required to strip the ISM from UGC 4459 is $n_{\rm IGM} \geqslant 8 \times 10^{-5}$ cm^{-3}. UGC 4459 is located at a projected separation of $\sim 8.4°$ (520 kpc) to the South-West of M81 (which we can take to be the center of the M81 group). The $n_{\rm IGM}$ required for ram pressure stripping of UGC 4459 is much higher than $n_{\rm IGM}$ expected at this location ($\sim 1.4 \times 10^{-6}$ cm^{-3}; assuming that 1% of the virial mass of the group is dispersed uniformly in a hot IGM within a sphere just enclosing UGC 4459; Bureau & Carignan (2002)). Hence, it seems unlikely that the peculiar kinematics of the galaxy is due to IGM ram pressure.

Given the kinematical asymmetry between the two halves of the galaxy, it is not surprising that a tilted ring fit does not give consistent results for the two halves. The difference in the peak velocities for the rotation curves derived from the two halves is ~ 15 km s^{-1}. This difference is significant compared to the peak value of 25 km s^{-1}obtained for the receding half of the galaxy. One can crudely estimate the maximum possible circular velocity in the following way; the velocity difference from one edge of the galaxy to the other is 18 km s^{-1}, this implies that the magnitude of any circular velocity component must be limited to $V_{\rm rot}\sin(i) \leqslant 9$ km s^{-1}.

Pustilnik et al.(2003) found substantial small scale velocity gradients in the Hα emission along a slit placed parallel to the optical major axis (i.e. also along the direction of maximum velocity gradient in the HI velocity field), as well as a large scale gradient, with magnitude somewhat larger than what we observe in the HI.

UGC 4459 has the largest star formation rate of all the galaxies in our sample. Pustilnik et al.(2003) estimate very young ages ($\sim 3 - 8$ Myr) for the star forming knots in the galaxy. Since they find no nearby galaxy that could have triggered this recent starburst, they suggest that it could be triggered by tidal interaction with the M81 group as a whole, or by interaction with the intra group medium. As we argued above, the ram pressure of the intra group medium is likely to be small. The velocity field of UGC 4459 is however qualitatively very similar to that of DDO 26 (Hunter & Wilcots (2002)) and IC 2554 (Koribalski et al.(2003)), both of which are suspected to be late stage mergers. It seems possible therefore that UGC 4459 too represents a recent merger of two still fainter dwarfs.

4.2.3 CGCG 269-049

CGCG 269-049 is an extremely metal poor dwarf galaxy with 12+log(O/H)$\sim$ 7.43 (Kniazev et al. (2003)). It is a member of the Canes Venatici I cloud. The optical emission in CGCG 269-049 shows two components, a central compact component and an outer faint extended component; both elongated in the northwest direction. The HI distribution of the galaxy also shows an elongation in the same direction. However, a misalignment of $\sim 10°$ is seen be-

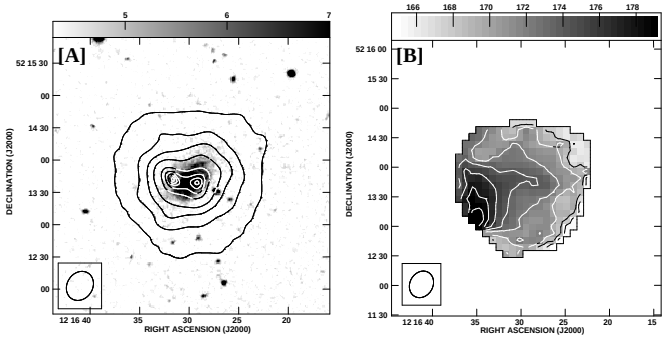

Figure 6. [A] The B band optical DSS image of UGC 7298 (greyscales) with the GMRT $26'' \times 24''$ resolution integrated HI emission map (contours) overlayed. The contour levels are 0.2, 2.7, 5.3, 7.9, 9.1, 10.5, 11.2 and 11.5 $\times 10^{20}$ atoms cm^{-2}. **[B]** The HI velocity field for galaxy at $26'' \times 24''$ resolution. The contours are in the steps of 2.0 km s^{-1}and range from 166.0 km s^{-1}to 180.0 km s^{-1}.

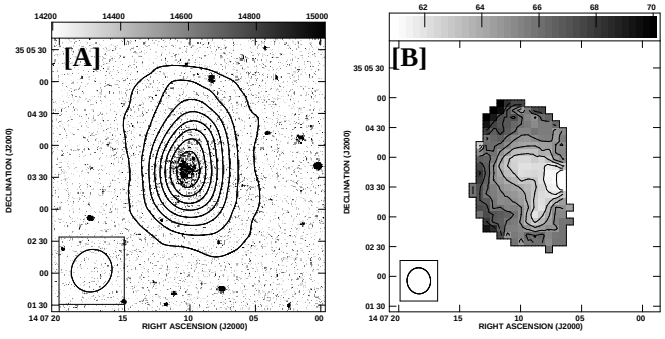

Figure 7. [A] The B band optical DSS image of KK 230 (greyscales) with the GMRT $48'' \times 45''$ resolution integrated HI emission map (contours) overlayed. The contour levels are 0.09, 0.50, 0.92, 1.33, 1.75, 2.16, 2.58, 3.00, 3.41 and 3.83 $\times 10^{20}$ atoms cm^{-2}. **[B]** The HI velocity field for galaxy at $26'' \times 24''$ resolution. The contours are in the steps of 1.0 km s^{-1}and range from 61.0 km s^{-1}to 68.0 km s^{-1}.

tween the optical and the HI major axis. The HI distribution is regular and shows a slightly off-centered peak; this signature is more prominent in the high resolution HI images.

CGCG 269-049 is undergoing a burst of star formation as indicated by strong emission lines in its spectra. It has been suggested that starbursts in dwarf galaxies could be triggered by tidal interaction with a companion (Taylor (1997), Walter & Brinks (2001)). While CGCG 269-049 does have a nearby companion (viz. UGC 7298 as discussed in Sect.4.2.4) the HI distribution in neither of these galaxies is suggestive of tidal interaction.

The velocity field of the galaxy shows a large scale gradient, roughly aligned with the morphological major axis and with a magnitude of ~ 5.2 km s^{-1}kpc^{-1} (Fig. 5[B]). Of all the galaxies in this subsample, CGCG 269-049 has a velocity field that most resembles that expected from a rotating disk. Substantial deviations from simple rotation can however be seen, and a tilted ring fit to the velocity field does not yield meaningful results. CGCG 269-049 has one of the highest current star formation rates among our sample galaxies; Hα imaging of this galaxy shows a bright Hα core near its center (see Fig. 9 & 12). From Fig. 5[B], one can see kinks in the velocity field in the regions near this star forming knot. Hence, it is likely that the energy input from the on-going star formation in the galaxy is responsible for at least some of the distortions seen in the velocity field. The maximum velocity difference from one edge of the galaxy to the other is ~ 16 km s^{-1}, hence $\mathrm{V_{rot}}\sin(i) \leqslant 8$ km s^{-1}.

4.2.4 UGC 7298

UGC 7298 is a member of the Canes Venatici I cloud of galaxies. The velocity field of UGC 7298 (Fig. 6[B]) shows a large scale gradient roughly aligned with the line joining the two high density gas clumps. The magnitude of the gradient is ~ 3.5 km s^{-1}kpc^{-1}. The velocity field is broadly similar to that in UGC 4459. The optical properties of the two galaxies are however very dissimilar. UGC 4459 is currently undergoing a starburst and its optical appearance is dominated by bright star forming knots. UGC 7298 on the other hand has a very small current star formation rate, as inferred from very faint Hα emission in the galaxy (Fig. 9 & 12). The maximum velocity difference from one edge of the galaxy to the other is ~ 16 km s^{-1}, implying that $\mathrm{V_{rot}}\sin(i) \leqslant 8$ km s^{-1}.

4.2.5 KK 230

KK 230, the faintest dwarf irregular galaxy in our sample, is yet another member of the Canes Venatici I cloud of galaxies (Karachentsev et al. (2003)). The velocity field (Fig. 7[B]) shows a gradient in the east-west direction (i.e. roughly perpendicular to the HI and optical major axis) with a magnitude of ~ 6 km s^{-1} kpc^{-1}. Even apart from this misalignment, the velocity field bears little similarity from that expected from a rotating axi-symmetric disk. The origin of the velocity gradient in KK 230 is rather puzzling. This galaxy has no measurable ongoing star formation, and no Hα emission was detected from the galaxy. It also lies at the periphery of the Canes Venatici I cloud group of galaxies; Karachentsev et al. (2004) found its tidal index to be -1.0, meaning that it is a fairly isolated galaxy. This, along with the fairly regular HI distribution make it unlikely that tidal forces are responsible for the observed velocity field. The maximum velocity difference from edge of galaxy to the other is ~ 10 km s^{-1}, which gives $\mathrm{V_{rot}}\sin(i) \leqslant 5$ km s^{-1}.

5 DISCUSSION

5.1 Dynamical mass of our sample galaxies

As discussed above, large scale systematic gradients are seen across all the newly mapped galaxies. In fact, all the 10 galaxies in our sample have velocity fields with a measurable ordered component, contrary to the general belief (e.g. Lo et al. (1993)) that the velocity fields of faint dwarf galaxies are "chaotic". Some of our sample galaxies overlap with those in Lo et al. (1993), and from a comparison of the new and old determinations of the velocity fields, it appears that high sensitivity and high velocity resolution (~ 1.6 km s^{-1}as opposed to the earlier used ~ 6 km s^{-1}) are crucial to discern systematic kinematical patterns in such faint galaxies.

The origin of these ordered fields is unclear. One would expect that in the absence of external forces, or internal energy input, gas with non zero angular momentum would settle down into a rotating disk. Tidal forces, and/or energy input from star formation could profoundly disrupt the gas velocity fields. Indeed it has often been

Table 4. Dynamical mass estimate for our sample galaxies

Galaxy	$\sigma_{\rm true}$ (km s^{-1})	$\Gamma_{\rm B}$	M_* ($10^6 M_\odot$)	$M_{\rm VT}$ ($10^8 M_\odot$)
KDG 52	8.5	0.6	3.7	1.5
UGC 4459	8.0	1.0	45.7	1.9
CGCG 269-049	9.0	1.0	15.0	1.2
UGC 7298	8.0	0.7	8.8	1.6
KK 230	7.0	1.0	1.0	0.5

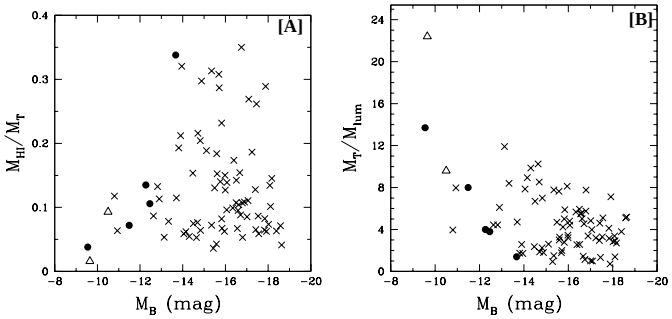

Figure 8. [A] M_{HI}/M_T as a function of M_B for a sample of dwarf irregular galaxies ($M_B \geqslant -19$). M_T is estimated from the last measured point of the rotation curve for Verheijen(2001), Swaters (1999) and Cote et al. (2000) (represented as crosses), whereas for galaxies from our sample (solid dots) and for LGS-3 and Sag DIG from Young & Lo (1997) (triangles), M_T is estimated from the virial theorem. **[B]** M_T/M_{lum} for the same sample. See text for more details.

suggested that a strong starburst could drive out the ISM of such small galaxies (see e.g. Dekel & Silk (1986), Efstathiau (2000), Ferrara & Tolstoy 2000). For two of the galaxies in our sample, viz. GR 8 (Begum & Chengalur (2003)) and KDG 52 (Puche & Westpfahl (1994)), detailed modeling shows that the velocity field can be fit by a combination of circular and radial motions of the gas. In general though, there does not seem to be any particular correlation between the current star formation rate (see Table 5) and the distortion of the velocity fields. For example, the velocity field of CGCG 269-049 (Fig.5[B]) shows relatively mild deviations from that expected from rotation, as compared to that of UGC 7298 (Fig. 6[B]), even though both galaxies have comparable luminosities and the star formation rate in CGCG 269-049 is more than an order of magnitude more than that of UGC 7298. Tidal interactions are also not clearly implicated, as several of our galaxies are relatively isolated, and none of them show morphologies typical of tidal interactions. Interestingly, some compact high velocity clouds (notably M 31 HVC 1, M 31 HVC 16; Westmeier et al.(2005)) show similar velocity gradients. Westmeier et al.(2005) argue against these velocity gradients being due to tidal forces, and suggest that they may be indicative of dark matter in these objects.

Given their peculiar kinematics, it is difficult to accurately determine the total dynamical mass of our sample galaxies. We instead compute an indicative dynamical mass using the virial theorem, assuming that the HI distribution is spherical and has an isotropic velocity dispersion and negligible rotation. We realize that these assumptions are unlikely to be rigorously justifiable in the current situation, and therefore this mass estimate is at best indicative. Under the assumptions above, the virial mass estimate is (e.g. Hoffman et al. (1996)):

$$M_{\rm VT} = \frac{5\, R_{\rm HI} \times \sigma^2_{\rm true}}{G} \qquad (3)$$

where $R_{\rm HI}$ is the HI radius of the galaxy at a column density of 10^{19} atoms cm^{-2} (from Table 3). $\sigma_{\rm true}$ is the HI velocity dispersion corrected for the instrumental broadening as well as for the broadening due to the velocity gradient over the finite size of the beam. This correction is applied using

$\sigma^2_{\rm true} = \sigma^2_{\rm obs} - \Delta v^2 - \frac{1}{2} b^2 (\nabla v_{\rm o})^2$,

where $\sigma_{\rm true}$ is the true velocity dispersion, Δv is the channel width, b characterizes the beam width (i.e. the beam is assumed to be of form e^{-x^2/b^2}) and $v_{\rm o}$ is the observed rotation velocity. $\sigma_{\rm obs}$ is the observed velocity dispersion in the HI gas given in Table 3.

Table 4 lists the estimated dynamical mass ($M_{\rm VT}$) for our sample galaxies. The columns in the table are: Col.(1) The galaxy name, Col.(2) The estimated $\sigma_{\rm true}$, Col.(3) The stellar mass-to-light ratio, $\Gamma_{\rm B}$ is obtained from the observed B$-$V colour for each galaxy, using the low metallicity Bruzual & Charlot SPS model for a stellar population with metallicity Z=0.008, a Salpeter IMF and an exponentially declining star formation rate of age 12 Gyrs (Bell & de Jong 2001). In absence of any colour information for CGCG 269-049, we assume $\Gamma_{\rm B}$=1 for it. Col.(4) The stellar mass obtained from the assumed mass-to-light ratio and Col.(5) The virial mass, as obtained from Eqn. 3.

Figure 8[A] is a plot of the ratio of HI mass to the dynamical mass against absolute blue magnitudes for a sample of dwarf irregular galaxies. The references from which the data are taken are listed in the figure caption. For our current sample, the dynamical masses are taken from Table 4, Begum et al.(2003), Begum & Chengalur (2004) (for KK 44 and DDO 210) and Young & Lo (1997) (for LGS-3 and Sag DIG). The ratio of $M_{\rm HI}/M_{\rm VT}$ for UGC 4459 is found to be $\sim$0.34, which is larger than a value typically seen in dwarf galaxies. Such high value of $M_{\rm HI}/M_{\rm VT}$ is also seen in some blue compact dwarf galaxies (e.g. van Zee et al. (1998)). Figure 8[B] shows $M_{\rm VT}/M_{\rm lum}$ for the same sample, plotted as a function of M_B. The luminous mass, $M_{\rm lum}$ is the sum of the stellar and gas mass. The stellar mass for all galaxies was computed in exactly the same way as for our sample galaxies; the gas mass is obtained by taking into account the contribution of primordial He i.e. $M_{\rm gas} = 1.4 \times M_{\rm HI}$. We note that although $M_{\rm VT}/M_{\rm lum}$ does not show any correlation with M_B for the full sample, there is a trend of an increase in the $M_{\rm VT}/M_{\rm lum}$ ratio with the decrease in M_B, seen in our sample galaxies. Further, a jump in $M_{\rm VT}/M_{\rm lum}$ ratio is seen at the faintest luminosities ($M_B > -10.0$). While this might be indicative of increased baryon loss from the halos of these galaxies (e.g. Gnedin et al. (2002)), we caution that there is considerable uncertainty in the dynamical mass for the galaxies in this magnitude range, and also that the total number of galaxies is too small to substantiate such a claim.

5.2 HI column density and star formation

Our sample galaxies have widely different star formation rates (see Table 5), and range from having no detectable on-going star formation (e.g. KK 230, KDG 52), to having an optical appearance that is dominated by bright star forming knots (e.g. UGC 4459, CGCG 269-049). As such, this is a well suited sample for trying to determine the connections (if any!) between the HI distribution and kinematics and star formation.

For spiral galaxies, the star formation rate appears to be quite well correlated with the gas column density, though it is unclear

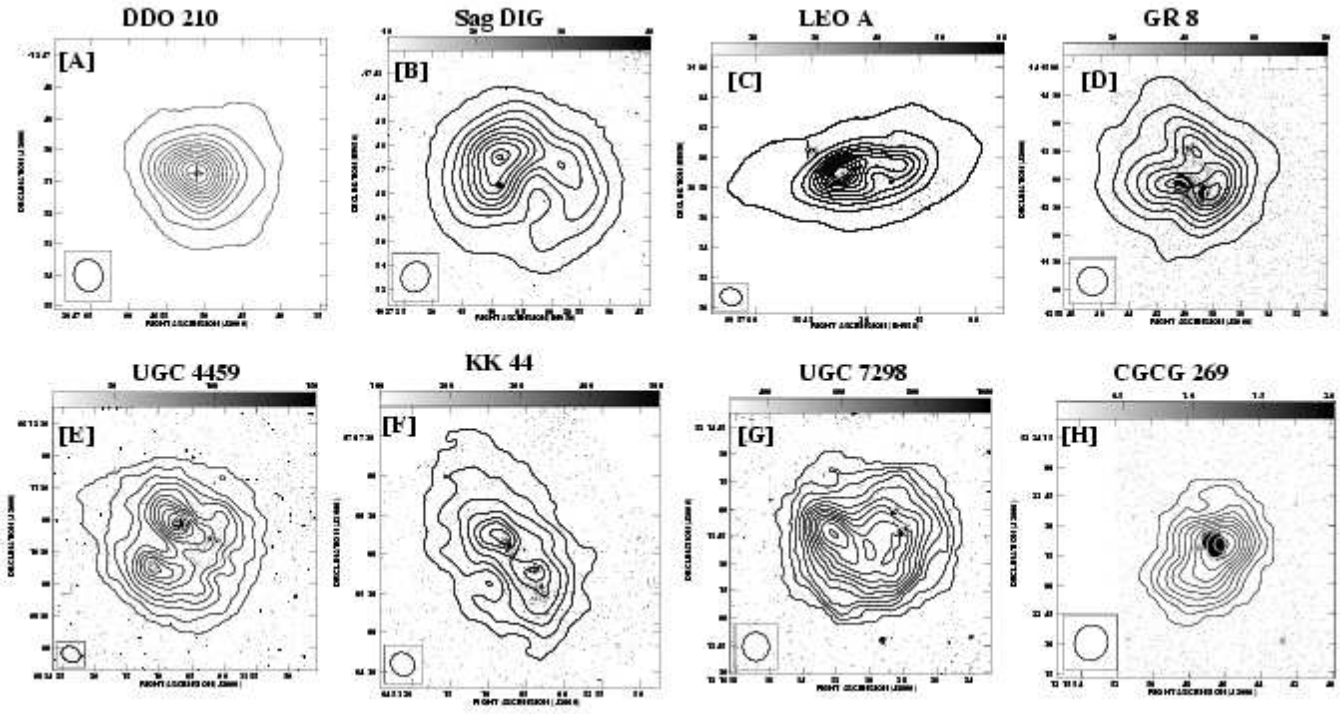

Figure 9. Comparison of integrated HI emission (contours) from the sample galaxies at a linear resolution of ∼300 pc with Hα emission (greyscales). The angular resolution of the HI images are given in Table 5. KK 230 and KDG 52 are not shown in the figure as no Hα was detected in these galaxies. In the case of DDO 210, the region of Hα emission found in the galaxy (van Zee 2000) is show as a star, however we note that this may not be an HII region. The Hα image of UGC 4459 is kindly provided by U. Hopp and is previously published by Schulte-Ladbeck & Hopp (1998). Hα images of Leo A, Sag DIG and GR 8 are obtained from NED. The observations of these galaxies is described in Hunter & Elemgreen (2004). For UGC 7298, CGCG 269-049 and KK 44 the alignment of the Hα images and radio images is done by comparing the continuum+Hα images with the optical DSS images. In case of Leo A and Sag DIG in the absence of continuum images, alignment of the Hα images and radio images is done using the coordinates of the HII regions from Strobel et al.(1991), whereas for GR 8 the coordinates of the HII regions were obtained from Hodge et al. (1989)

if the gas column density is the only relevant parameter, as in the Schmidt law, or whether a combination of gas column density and the dynamical time are important, (as in the Toomre's instability criteria, see Kennicutt (1998)). For dwarf irregular galaxies, it has been suggested that star formation occurs only above a critical threshold column density ($\sim 10^{21}$ cm^{-2}, when measured at a spatial resolution of $\sim$ 500 kpc) and that this may be because a critical amount of dust shielding is required before star formation can commence (Skillman (1987)). Since the observed column density is resolution dependent and that the distance of our sample galaxies varies from 0.70 Mpc (Leo A) to 4.2 Mpc (UGC 7298), one would require maps at angular resolutions varying by a factor of $\sim$ 6. This problem is well suited to a telescope like the GMRT, where because of the hybrid configuration, maps at a range of angular resolutions can be made from a single observing run. For all our galaxies, we produced CLEANed HI maps at an angular resolution corresponding to a linear scale of $\sim$ 300 pc at the distance to the galaxy. We thus have a unique data set which spans a wide range of star formation rates, but for which maps are available at a similar linear resolution. The results from a comparison of the HI distribution with the sites of Hα emission are given in Table 5. Col.(1) shows the galaxy name, Col.2) the absolute blue magnitude (M_B) of the galaxy, Col.3) the resolution of the HI column density map, Col.4) the corresponding linear resolution in pc, Col.5) the observed HI peak column density, Col.6) the peak gas surface density. The gas surface densities are obtained by correcting the observed HI column densities for inclination and for primordial He content (which we take to be 10% of HI by number). Note that the peak gas density need not occur at the center of the galaxy, Col.7) the column density of the HI contour that just encloses all the HII emission in the galaxy, Col.8) current star formation rate (for KDG 52 & KK 230 the limits on the star formation rate are listed), Col.9) the metallicity of the galaxy (for some of our sample galaxies no measurement of the metallicity exist) and Col.(10) references for the star formation rate and the metallicity.

DDO 210 and KK 44 are the only galaxies in our sample which show systematic rotation; the rotation curves of these galaxies have been presented in Begum et al.(2003) (KK 44) and Begum & Chengalur (2004) (DDO 210). For these two galaxies we show in Fig. 10, the ratio of the azimuthally averaged gas density to the threshold density predicted from Toomre's instability criterion. For both of these dwarf galaxies, this ratio is everywhere smaller than the threshold ratio for star formation in spiral galaxies ($\Sigma_g/\Sigma_{crit} \sim 0.7$; Kennicutt (1989)). A similar result was obtained by van Zee et al.(1997), albeit for brighter (and more rotation dominated, $V/\sigma > 5$) dwarfs. While this low ratio of gas density to critical density is interesting, it is unclear whether the Toomre's instability criteria is relevant in a situation where the rotation speed is comparable to the velocity dispersion.

From the Hα overlays, one can see that if there does exist a threshold HI column density for star formation, it is only in the very loose sense that one can find a (relatively) high HI column

Table 5. Comparison of HI and optical emission from the sample galaxies

Galaxy	M_B	Beam (arcsec)	Beam (pc)	N_{HI}^{Peak} (10^{21} cm^{-2})	Σ_g^{peak} (10^{21} cm^{-2})	Σ_{HI}^{c}(HII) (10^{21} cm^{-2})	Log[SFR] ($M_\odot yr^{-1}$)	12+log(O/H)	References
KK 44	-11.85	19	307	1.0	0.6	0.4	-3.44		9
Leo A	-11.36	78	262	2.1	1.4	0.8	-3.68	7.3	2,8
KDG 52	-11.49	16	275	0.6	0.8	–	> -5.1		9
UGC 4459	-13.37	18	310	3.2	3.9	1.6	-2.04	7.52	6
CGCG 269-049	-12.46	18	297	2.4	2.5	1.7	-3.08	7.43	3,9
UGC 7298	-12.27	15	306	1.5	1.9	0.8	-4.5		9
GR 8	-12.11	30	305	1.1	1.4	0.9	-2.46	7.68	4
KK 230	-9.55	33	304	0.5	0.4	–	> -5.53		9
Sag DIG	-11.49	67	325	0.6	0.7	0.6	-3.56	7.42	1,7
DDO 210	-11.09	61	291	1.07	1.3	1.2	-5.42	7.4	5,8

References: 1-Hunter & Elmegreen(2004), 2-James et al.(2004), 3-Kniazev et al.(2003), 4-Legrand et al.(2001), 5-Mateo (1998), 6-Pustilnik et al.(2003), 7-Skillman et al.(1989), 8-Taylor et al.(1998), 9-This paper.

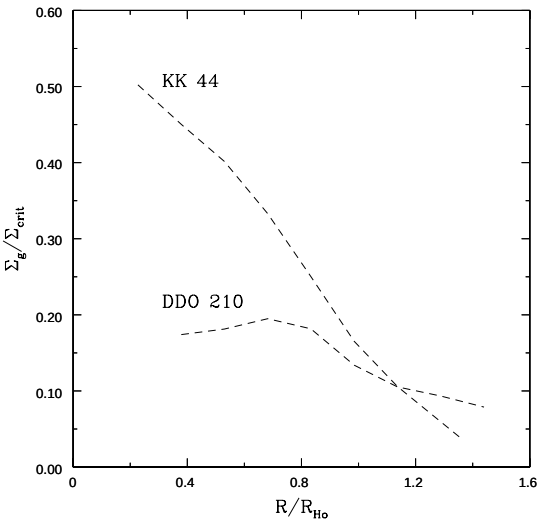

Figure 10. The ratio between the gas surface density and the Toomre's instability threshold density for our sample galaxies DDO 210 and KK 44, which show systematic rotation. The HI distribution used for deriving the SMD profiles are $61'' \times 56''$ (DDO 210) and $31'' \times 29''$ (KK 44).

density contour that just encloses all the star forming regions. The actual value of the column density delineating the star forming regions varies by more than a factor of 4 between different galaxies in our sample. Further, the morphologies of the Hα emission and the high column density HI is quite dissimilar in several cases (e.g. UGC 7298, GR 8, KK 44). Thus, while high HI column density may be necessary for star formation, it clearly is not, in this sample at least, a sufficient criteria for star formation. From Table 5 one can also see that there is no particular correlation between the "threshold" column density and the metallicity. The metallicity of our sample galaxies is somewhat lower than that in the original sample of Skillman (1987). In that sample the galaxies, with one exception (Sextans A, with $12 + \log(O/H) = 7.49$ (Kunth & Östlin (2000)), have $12 + \log(O/H)$ between ~ 8 and 8.34. For the galaxies in our sample for which measurements exist, the metallicity is typically 1 dex lower, while the star formation "threshold" density is similar to that noted by Skillman (1987). It has also been suggested that the threshold density for star formation is more related to the presence of a cold phase; in this case, the value of this threshold does not change much with metallicity (Schaye (2004)).

To further explore the connection between the amount of high column density gas in the galaxy and the star formation, we show in Fig. 11[A] and Fig. 11[B], the star formation rate as a function of the total HI mass as well as the star formation rate as a function of the mass of HI which has a column density greater than the "threshold" density defined in Table 5. The SFR rate actually correlates slightly better with the total HI mass of the galaxy (correlation coefficient ~ 0.34, excluding those galaxies where no Hα emission was detected) as compared to the mass of the gas at high HI column density (correlation coefficient ~ 0.25). Clearly, the efficiency with which gas is converted into stars in these dwarf galaxies is not a function of the amount of high column density of the gas alone. The strongest correlation between the gas distribution and indicators of current or past star formation that we find in our sample is that between the peak gas density (recall that this need not occur at the center of the galaxy) and the absolute magnitude (Fig. 11[C]). The reason for the existence of such a correlation is unclear. The most straight forward interpretation is that bigger galaxies are more able to support high column density gas; this in turn made them, on the average, more efficient at converting their gas into stars. On the other hand, as noted above, the current star formation rate itself does not correlate particularly strongly with the local column density. One way to reconcile this would be if in such small galaxies, feedback processes rapidly destroy the correlation between the local gas column density and the local star formation rate.

If feedback from star formation is important, one might expect to see the strongest evidence for this on small scales. We hence compare the highest resolution HI images of our sample galaxies with the sites of active star formation i.e. Hα emission. Our highest resolution images have beam sizes $\sim 3'' - 4''$, which corresponds to linear scales between 19 pc and 100 pc for our sample galaxies. At this high resolution, the emission could not be CLEANed; moment maps were instead made from the dirty cubes. As discussed earlier, this leads to a scaling uncertainty, which means we cannot translate the observed flux distributions into corresponding HI column densities. We can however, still use our maps to search for correspondences between the morphologies of the Hα and the high column density HI. The overlays are shown in Fig. 12; for all the galaxies in our sample, the HI emission shows substantial fine scale

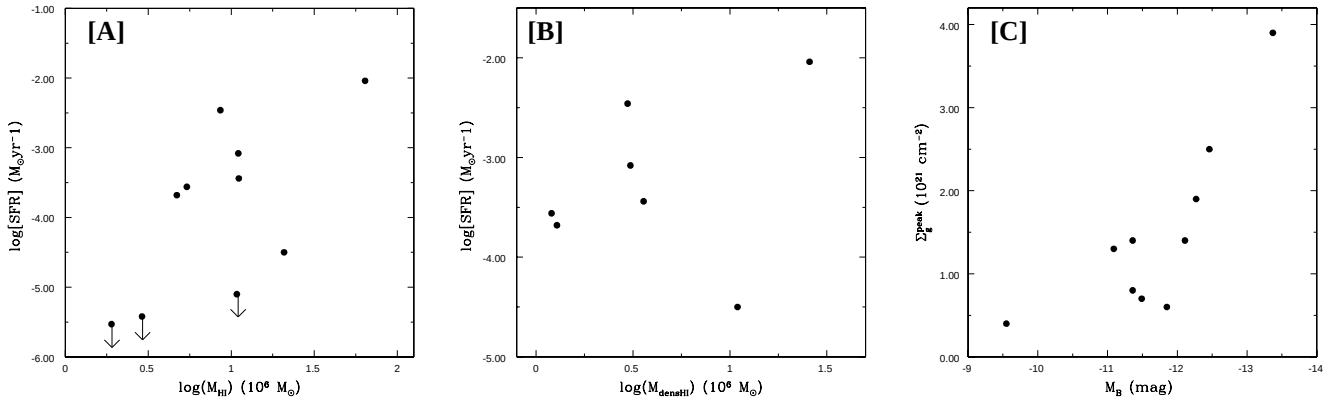

Figure 11. [A] Log of HI mass as a function of SFR for our sample galaxies. In the case of KDG 52, KK 230 and DDO 210, the limits on the SFR are shown. **[B]**HI mass of the dense gas i.e mass of HI gas which has a column density greater than the "threshold" density, defined in Table 5, as a function of SFR for the same sample. **[C]** The peak surface gas density as a function of absolute blue magnitude.

structure, with shell like, filamentary as well as discrete clump like morphologies being visible. The few other dwarf galaxies that have been imaged at similar linear scales, e.g. IC10 (20 pc; Wilcot & Miller (1998)), SMC (28 pc; Staveley-Smith et al. (1997)), LMC (15 pc; Kim et al. (2003)) also show a similar wealth of small scale structure. At these scales, the Hα emission is sometimes seen coincident with high HI column densities (e.g. the northern star forming region in UGC 4459, north-eastern region in KK 44, the Hα knot in CGC 269-049), sometimes the high HI column density gas forms a shell around the Hα emission (e.g. the south-western star forming region in KK 44, the high density HI clumps in GR 8) and sometimes there seems to be no connection at all between the high density HI gas and the Hα emission (e.g. UGC 7298). In general, while high HI column density gas is in general present in the vicinity (as measured on linear scales < 100 pc) of current star formation, there does not seem to be a simple, universal relationship between the Hα emitting gas and the high column density neutral gas.

5.3 HI line profiles and star formation

Young and collaborators have found that in faint dwarfs, HI line profiles in regions of active star formation differ substantially from a simple Gaussian shape (Leo A, Young & Lo 1996; Sag DIG, Young & Lo 1997; UGCA 292 Young et al. 2003). Young et al.(2003) used both a two Gaussian fit as well as a fit using Gauss-Hermite polynomials to parametrize the line profiles. To facilitate easy comparison, we fit the line profiles to our sample galaxies using the same two models. Apart from Leo A and Sag DIG (where we use essentially the same VLA data as used by Young et al.) our sample has two galaxies, viz. DDO 210 and GR 8, in common with the earlier sample. We include these two galaxies in the analysis that we do in this section, and compare the results obtained from the GMRT data with those obtained earlier with the VLA.

Ideally one would like to fit profiles to data cubes which correspond to the same linear resolution at the distance to the galaxy. However fitting to the line profile requires a good signal to noise ratio, and for the fainter galaxies, the signal to noise ratio is adequate only in the lowest resolution images. The linear resolution of the data cubes used for profile fitting is given in Table 6. For all the sample galaxies, the line profiles at each location were first fitted with a single Gaussian component and the residuals were inspected. HI profiles in some cases were found to deviate measurably from a simple Gaussian $-$ in such cases the profiles were often either asymmetric or symmetric, but with narrower peak and broader wings than a Gaussian.

The profiles were then fit with a double Gaussian and also separately with a Gauss-Hermite polynomial. The Gauss-Hermite polynomial used for the profile fitting is given as:

$$\phi(x) = ae^{\frac{-1}{2}y^2}[1+\frac{h_3}{\sqrt{6}}(2\sqrt{2}y^3-3\sqrt{2}y)+\frac{h_4}{\sqrt{24}}(4y^4-12y^2+3)] \quad (4)$$

where y= $\frac{(x-b)}{c}$. Parameters a, b, c are equal to the amplitude, mean and dispersion respectively for a Gaussian (to which the Eqn.(4) reduces to, when parameters h_3 and h_4 are zero). Parameter h_3 is related to the skewness of the line profile i.e. in the case of an asymmetric line profile $h_3 \neq 0$. If $h_4 \neq$0, the line profiles either have a more pointed top with broader wings ($h_4 > 0$) or have a flatter top ($h_4 < 0$) than a Gaussian.

In the case of Gauss-Hermite fits, the profiles for which both h_3 and h_4 parameters were less than 3 times the uncertainty in these parameters, were rejected as bad fits. Similarly, in the case of double Gaussian fit, the profiles for which the width of the fitted narrow component was less than the velocity resolution of 1.65 km s^{-1}(within the errorbars) were rejected. Following Young & Lo (1996), we use the F-test to distinguish between profiles that are adequately fit by a single Gaussian and those which are not. Locations where the null hypothesis (viz. that a single Gaussian provides an equally good description of the line profile as compared to a double Gaussian or Gauss-Hermite polynomial) was rejected at the 90% or higher confidence level were compared with the locations of ongoing star formation.

The results of the line profile fitting are given in Table 6. Col.(1) gives the galaxy name, Col.(2) shows the resolution of the HI distribution used for the profile fitting, Col.(3) the liner resolution in pc, Col.(4) the minimum gas surface density (the observed HI column density corrected for inclination and He content) enclosing the regions with non Gaussian HI profiles, Col.(5) h_3 and h_4 parameters of the best fit Gauss-Hermite polynomial, Col.(6) range of the velocity dispersion of the narrow component in the double Gauss fit and Col.(7) range of the velocity dispersion of the broad component in the double Gauss fit. In case of UGC 4459 and GR 8,

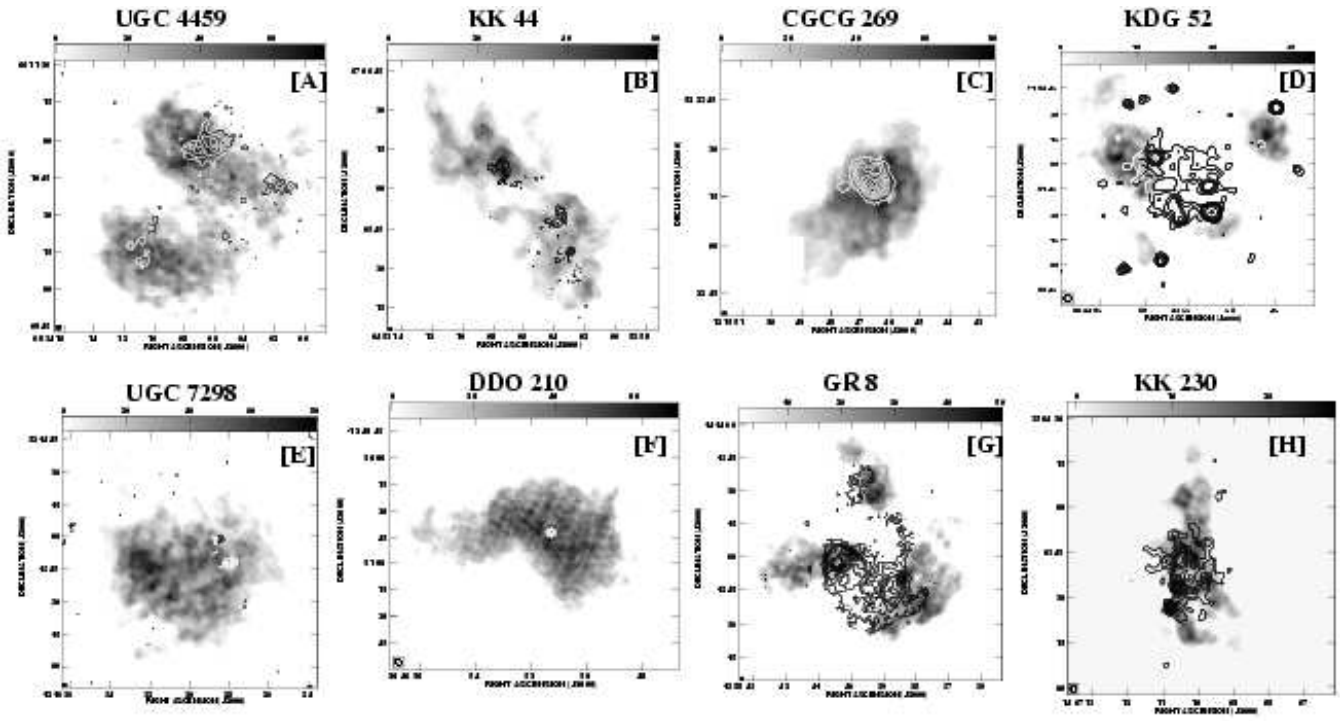

Figure 12. The GMRT integrated high resolution HI images of our sample galaxies (greyscales) overlayed on Hα images (contours). In case of KK 230 and KDG 52, as no Hα emission was detected, contours represent the optical broad band emission. The angular resolutions of the GMRT HI images are $3'' \times 3''$ (UGC 4459), $4'' \times 4''$ (KK 44), $4'' \times 3''$ (CCG 269-049), $6'' \times 6''$ (KDG 52), $4'' \times 4''$ (UGC 7298), $4'' \times 3''$ (DDO 210), $4'' \times 3''$ (GR 8) and $4'' \times 3''$ (KK 230). The source of Hα emission found in DDO 210 (van Zee 2000) is show as a star.

results of the line profile fitting from separate regions (as marked in the Fig. 13), are described separately in the Table 6. For KDG 52, the two separate regions showing deviation from the Gaussian, near the eastern and western clump, gave similar results.

The regions in our sample galaxies where the double Gaussian gave a better fit to the line profiles than a single Gaussian are marked as crosses on the HI column density distribution in Fig. 13. The regions where the Gauss-Hermite polynomial gave a better fit than the single Gaussian are almost similar to the regions where the double Gaussian gave a good fit, hence are not shown separately. We note that for most galaxies (with the exception of DDO 210) the extent of these regions is comparable to our spatial resolution. To allow easy cross comparison with regions having on-going star formation, the Hα emitting regions are represented as greyscales in Fig. 13. The line profiles for KK 44 and KK 230 throughout the galaxy are found to be well described by a single Gaussian component, hence are not shown.

As seen in Fig. 13, no particular correlation is seen between the location of Hα emission and the deviation of HI line profiles from single Gaussians. Not all star forming regions in our sample galaxies show deviation of the line profiles e.g. UGC 7298, KK 44 and eastern clump in GR 8. Conversely, not all regions which show deviations of line profiles are associated with the star forming regions e.g. KDG 52, DDO 210 and UGC 7298. In this sample at least, the correlation found by Young et al.(2003) from their analysis of 3 dwarf irregular galaxies does not seem to hold. We also do not find any correlation between the presence of asymmetric profiles and the global star formation activity.

The dwarf galaxies DDO 210 and GR 8 are common between our sample and that of Young et al.(2003). The results derived by Young et al.(2003) for DDO 210 are similar to our results. On the other hand, for GR 8, Young et al.(2003) found few line profiles with $h_3 \neq 0$ in the southern clump, (albeit with a very small magnitude of h_3), and almost none in the eastern clump, while we found all the profiles associated with the southern and eastern clump have $h_3 = 0$, (within the 3σ uncertainty of the parameter). However, this difference is not pronounced, and one should also note that Young et al.(2003) used $14'' \times 14''$ and $18'' \times 18''$ resolution data cubes, whereas we have used a $30'' \times 30''$ resolution data cube. In general hence, there is relatively good agreement between the fits obtained with the GMRT and VLA data.

6 SUMMARY

We compare the HI distribution, kinematics and current star formation in a sample of 10 extremely faint nearby dwarf galaxies. For 5 of these galaxies, fresh GMRT HI data are presented in this paper. The large scale gas distribution in the galaxies is generally clumpy, and the peak HI column density is often well removed from the geometric center. For all galaxies we find a large scale ordered velocity field, although the patterns are mostly not reconcilable with that expected from a rotating disk. From a simplistic virial theorem based estimate of the dynamical mass, we find very tentative evidence that the faintest dwarf irregulars have a somewhat smaller baryon fraction than brighter galaxies.We compare the regions of ongoing star formation with regions of high HI column density, with the column density being measured at a uniform linear scale (~ 300 pc) for all galaxies in our sample. We find that while the Hα emission is confined to regions with relatively high column density,

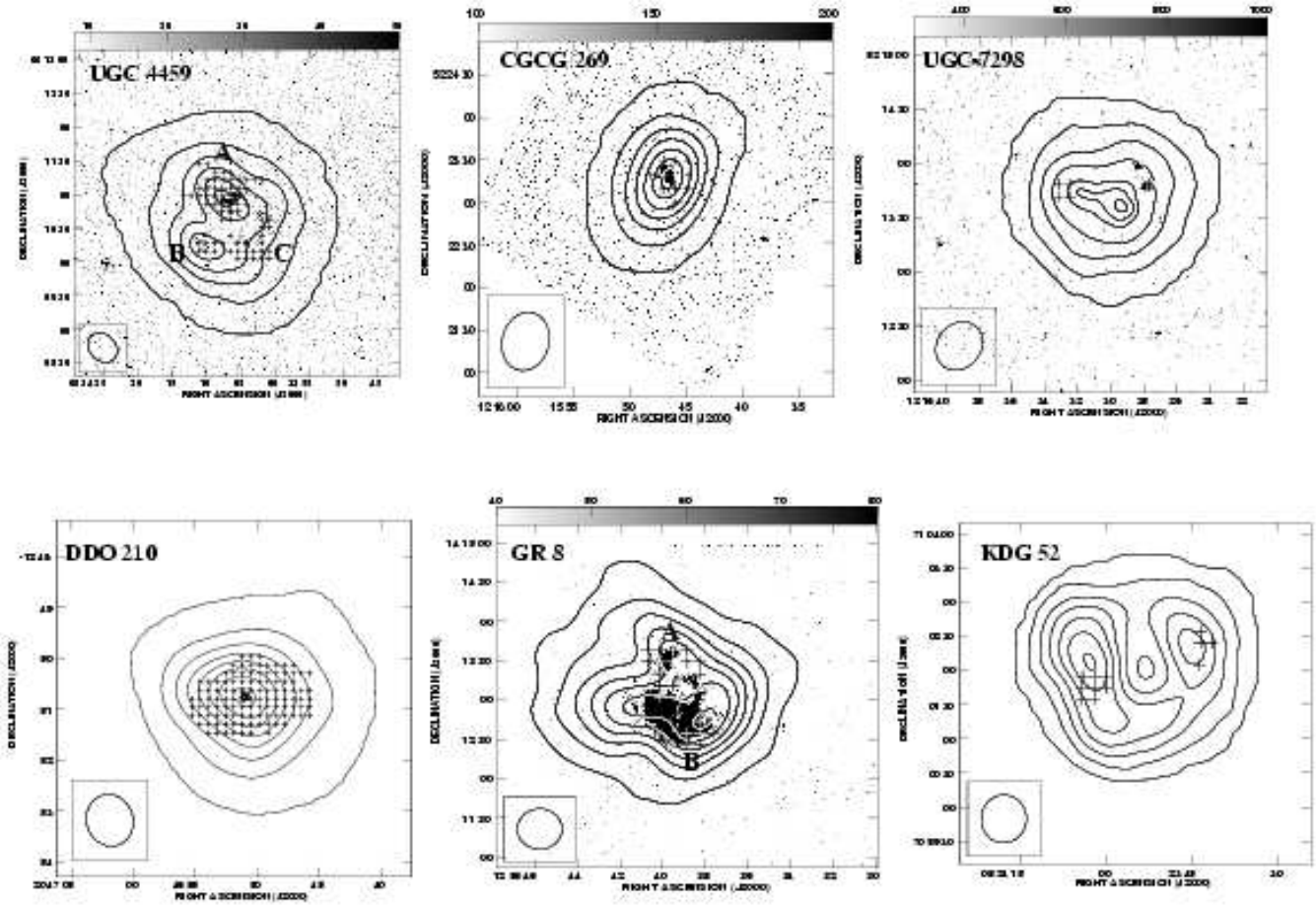

Figure 13. GMRT integrated HI column density distribution for our sample galaxies (contours) overlayed on the Hα emission (greyscale) from the galaxies. The regions where the line profile deviated from the single Gaussian are marked as crosses. In the case of DDO 210, the HII region the galaxy is marked as stars. In case of KDG 52, no Hα emission was detected in the galaxy. The resolution of the HI distribution are $29'' \times 27''$ (UGC 4459), $42'' \times 39''$ (CGCG 269-049), $28'' \times 24''$ (UGC 7298), $60'' \times 58''$ (DDO 210), $30'' \times 30''$ (GR 8) and $42'' \times 39''$ (KDG 52).

Table 6. Results of the profile fitting to our sample galaxies

Galaxy	Beam (arcsec)	Linear resolution (pc)	Σ^{c}_{gas} (10^{21} cm^{-2})	Gauss-Hermite fit	Narrow component (km s^{-1})	Broad component (km s^{-1})
KK 44	40	647	–	–	–	–
KDG 52	42	723	0.2	$h_3 = 0\ h_4 > 0$	2.0−4.5	8−14
UGC 4459 (A)	26	450	1.0	$h_3 < 0\ h_4 = 0$	3.5−7.0	6−17
UGC 4459 (B)	26	450	2.0	$h_3 = 0\ h_4 > 0$	6.0	10−17
UGC 4459 (C)	26	450	1.0	$h_3 = 0\ h_4 > 0$	4.5−6.0	10−16
CGCG 269-049	42	692	0.4	$h_3 < 0\ h_4 = 0$	2−5	7−13
UGC 7298	26	529	1.0	$h_3 = 0\ h_4 > 0$	2.5−4	9.5−11
GR 8 (A)	30	305	0.7	$h_3 < 0\ h_4 > 0$	2−6	7−13
GR 8 (B)	30	305	0.9	$h_3 = 0\ h_4 > 0$	2−3	8−9.5
KK 230	48	489	–	–	–	–
DDO 210	60	291	0.4	$h_3 = 0\ h_4 > 0$	3−6	8−14

in general the morphology of the Hα emission is not correlated with that of the high column density HI gas. Thus, while high gas column density may be a necessary condition for star formation, it is not, in this sample at least, a sufficient condition. We also examine the line profiles of the HI emission, and check if deviations from a simple Gaussian profile is correlated with star formation activity. We do not find any such correlation in our sample – there are regions with on-going star formation but with simple Gaussian line profiles, as well as regions with complex line profiles but no ongoing star formation. Finally, we look at the distribution of HI gas at linear scales $\sim 20 - 100$ pc. All our sample galaxies show substantial small scale structures with shell like, filamentary as well as clumpy features being identifiable in the images. Hα emitting regions are sometimes associated with clumpy features; sometimes the Hα emission lies inside a shell like feature in the HI, and sometimes there is no particular HI column density enhancement seen near the Hα emission. The interplay between star formation and gas density and kinematics in these galaxies hence appears to be very varied, and the general unifying patterns seen in larger irregulars and spiral galaxies seem to be absent. Star formation and feedback are complex processes, and perhaps it is the presence of simple large scale correlations in big galaxies that should surprise us more than the absence of such correlations in small galaxies.

ACKNOWLEDGMENTS

We would like to thank Dr U. Hopp for providing the optical images of UGC 4459 and Dr S. Pustilnik for useful discussion on UGC 4459. AB thanks the Kanwal Reiki Scholarship of TIFR for partial financial support. The observations presented in this paper would not have been possible without the many years of dedicated effort put in by the GMRT staff in order to build the telescope. The GMRT is operated by the National Center for Radio Astrophysics of the Tata Institute of Fundamental Research.

REFERENCES

Begum, A., & Chengalur, J. N. 2004, A&A, 413, 525
Begum, A., Chengalur, J. N. & Hopp, U. 2003, New Astronomy, 8, 267
Begum, A., & Chengalur, J. N. 2003, A&A, 409, 879
Bell E. F., & de Jong, R. S., 2001, ApJ 550, 212.
Braine, J. Duc, P. A., Lisenfeld, U., Charmandaris, V., Vallejo, O., Leon, S. & Brinks, E., 2002, Ap&SS, 281, 407
Bureau, M., Walter, F., van Gorkhom, J. & Carignan, C., 2004, IAU Symposium series, Vol 217, 452
Bureau, M. & Carignan, C., 2002, AJ, 123, 1316
Côté, S., Carignan, C. & Freeman, K. C. 2000, Ap.J, 120, 3027
Dekel, A. and Silk, J. 1986, ApJ, 303, 39
de Vaucouleurs, G. & Moss, C., 1983, ApJ, 271, 123
Efstathiou, G. 2000, MNRAS, 317, 697
Ferrara, A. & Tolstoy, E. 2000, MNRAS, 313, 291
Gnedin, O.Y. & Zhao, H., 2002, MNRAS, 333, 299
Grebel, E. K., 2005, AIP Conference Proceedings , New York: American Institute of Physics, 752, 161
Grebel E. K., 2004, Carnegie Observatories Centennial Symposia, 237.
Gunn, J. E. & Gott, J. R. III, 1972, ApJ, 176, 1
Hodge, P., Lee, M.G. & Kennicutt, R. 1989, PASP, 101, 640
Hoffman, G.L., Salpeter, E.E., Farhat, B., Roos, T., Williams, H. & Helou, G, 1996, ApJS, 105, 269
Hunter, D. A. & Elmegreen, B. G., 2004, AJ, 128, 2170
Hunter D. A., Wilcots E. M., 2002, AJ, 123, 2449
James et al., 2004, A&A, 414, 23
Jörsäter S. & van Moorsel G. A.,1995, AJ, 110, 2037
Karachentsev, I. D., Karachentseva, V.E., Huchtmeier, W.K. & Makarov, D.I., 2004, AJ, 127, 2031
Karachentsev, I. D. et al., 2003, A&A, 398, 467
Karachentseva, V. E., & Sharina M.E. 1988, Communic. of SAO, 57, 5
Karachentseva, V. E., 1968, Soobshch.Byurakan Obs., 39, 62
Kennicutt R. C., 1998, ApJ, 498, 541
Kennicutt R. C., 1998a, ARA&A, 36, 189
Kennicutt, R. C., 1989, ApJ, 344, 685
Kim, S., Staveley-Smith, L., Dopita, M. A., Sault, R. J., Freeman, K. C., Lee, Y., & Chu, Y., ApJS, 148, 473
Kniazev, A. Y., Grebel, V. K., Hao, L., Strauss, M. A., Brinkmann, J. & Fukugita, M., 2003, ApJ, 593, L73
Koribalski B., Gordon S., Jones K., 2003, MNRAS, 339, 1203
Kunth, D. & Östlin, G., 2000, A&AR, 10,1
Lee, M. G.& Kim, S. C., 2000, AJ, 119, 777
Lee, M. G., Aparicio, A., Tikonov, N., Byun, Y. & Kim, E., 1999, AJ, 118, 853.
Legrand, F, Tenorio-Tangle, G., Silich, S., Kunth, D. & Cervino, M., 2001, ApJ, 560, 630
Lo, K. Y., Sargent, W. L. W. & Young, K. 1993, Ap.J., 106,507
Lo, K. Y. & Sargent, W. L. W. 1979, ApJ, 227,756
Majewski S. R., Skrutskie M. F., Weinberg M. D., Ostheimer J. C., 2003, ApJ, 599, 1082
Makarova, L., 1999, A&AS, 139, 491
Mateo, M., 1998, ARA&A, 36, 435
Puche, D. & Westpfahl, D., 1994, Proceedings of an ESO/OHP Workshop on Dwarf galaxies, edited by Georges Meylan and Phillippe Prugniel., p.273
Pustilnik, S., Zasov, A., Kniazev, A., Pramskij, A., Ugryumov, A. & Burenkov, A., 2003, A&A, 400, 841
Rupen, M. P., 1999, ASP Conf. Ser. 180: Synthesis Imaging in Radio Astronomy II, 229
Sargent, W. L. W., Sancisi, R. & Lo, K. Y., 1983, ApJ, 265, 711
Schaye J., 2004, ApJ, 609, 667
Schlegel, D. J., Finkbeiner, D. P. & Davis, M., 1998, ApJ, 500, 525
Schulte-Ladbeck, R. E. & Hopp, U., 1998, AJ, 116, 2886
Simpson, C. E., Hunter, D. A. & Knezek, P. M., 2005, AJ, 129, 160
Skillman, E. D., Kennicutt, R. C. & Hodge, P. W., 1989, ApJ, 347, 875
Skillman, E. D., Terlevich, R., Teuben, P. J., & H. van Woerden. 1988, A&A, 198, 33.
Skillman, E. D., 1987, in Star Formation in Galaxies, edited by C. J. Lonsdale Persson, NASA, 263
Staveley-Smith, L., Sault, R. J., Hatzidimitriou, D., Kesteven, M. J. & McConnell, D.,1997, MNRAS, 289, 225
Strobel, N. V., Hodge, P. & Kennicutt JR, R. C., 1991, ApJ, 383, 148.
Swarup, G., Ananthakrishnan, S., Kapahi, V. K., Rao, A. P., Subrahmanya, C. R., & Kulkarni, V. K. 1991, Current Science, 60, 95
Swaters, R. 1999, Ph.D. thesis, Rijksuniversiteit Groningen.
Taylor, C. L., Kobulnicky, H. A. & Skillman, E. D., 1998, AJ, 116, 2746

Taylor, C. L., 1997, ApJ, 480, 524
Tolstoy, E., Gallagher, J. S., Cole, A. A., Hoessel, J. G., Saha, A., Dohm-Palmer, R. C., Skillman, E. D., Mateo, M. & Hurley-Keller, D., 1998, AJ, 116, 1244
Toomre, A. 1964, ApJ, 197, 551
van Zee, L. 2000, AJ, 119, 2757
van Zee, L., Skillman, E. D. & Salzer, J. J., 1998, AJ, 116, 1186
van Zee, L., Haynes, M. P., Salzer, J. J. & Broeils, A. H., 1997, AJ, 113 1618
Verheijen, M.A.W. 2001, ApJ, 563, 694
Walter, F. & Brinks, E., 2001, AJ, 121, 3026
Westmeier T., Braun R., & Thilker D., 2005, A&A, 436, 101
Westpfahl, D., Coleman, P. H., Alexander, J. & Tongue, T., 1999, AJ, 117, 868
Wilcots, E. M. & Miller, 1998, AJ, 116, 2363
Young, L. M., van Zee, L., Lo, K. Y., Dohm-Palmer, R. C. & Beierle, M. E., 2003, ApJ, 592, 111
Young, L. M. & Lo, K. Y., 1997, ApJ, 490, 710
Young, L. M. & Lo, K. Y., 1996, ApJ, 462, 203